Supplementary Materials: Air Quality in the Italian Northwestern Alps during Year 2020: Assessment of the COVID-19 «Lockdown Effect» from Multi-Technique Observations and Models

Henri Diémoz, Tiziana Magri, Giordano Pession, Claudia Tarricone, Ivan Karl Friedrich Tombolato, Gabriele Fasano, and Manuela Zublena

S1. Considerations on the time span for calculation of the reference average

In order to calculate, for each of the lockdown phases examined, an average of the concentrations measured in the years prior to 2020, to be used as a reference (counterfactual) scenario representative of business-as-usual conditions (Sect. 3.1), an averaging time span must be carefully chosen. This interval must be:

1. short enough, to ignore any long-term trend, both in the pollutant emissions and in the meteorological conditions, present in the data set (or assume that natural variability has a larger effect) and not to introduce a bias in the calculation of the 2020 anomaly [1];
2. sufficiently long, in order for the average value to be representative of mean conditions and not much impacted by the anomalous meteorology in a specific year.

A brief study is therefore carried out to assess the optimal time span, based on the two points above.

First of all, we consider the effect of possible trends (point 1). To this end, we use, as an example, the series of NO_2 surface concentrations in Donnas, i.e. one of our longest data sets according to Table 1 (main text) and characterised by a clear long-term trend due to improvements in air quality. A Theil-Sen test [2] is applied on the deseasonalised data set. The results are presented in Fig. S1. The trend amounts to -1.05 µg m^{-3} year^{-1} and is highly significant ($p < 0.001$). This means that if we do not want to introduce an error larger than a few µg m^{-3} (which is approximately the expected concentration decrease during P2) on the calculation of the reference average, a time span longer than, e.g., 5 years is not recommended.

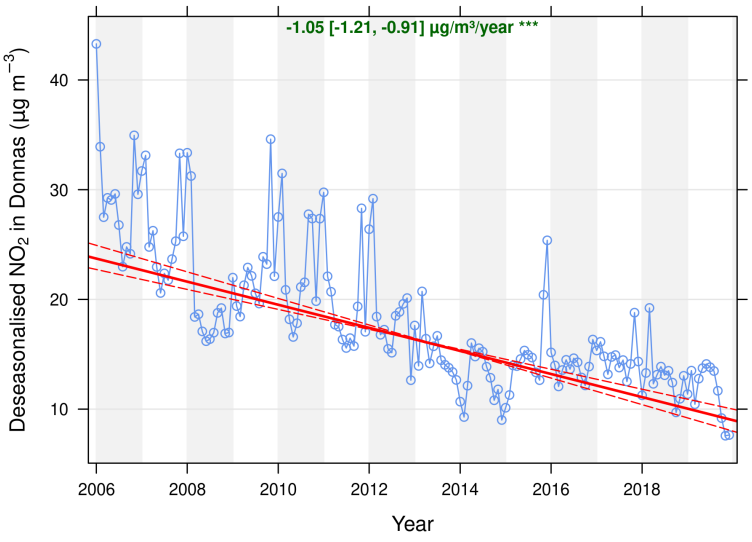

Figure S1. Deseasonalised NO_2 series in Donnas (cyan) and results of the Theil-Sen test (red).

Besides (second point), the averaging time should be long enough to avoid strong influence by anomalous meteorological conditions on surface concentrations. In order to quantify the "roughness" of the data set resulting from averaging over different time spans, we develop the following metrics. We first average together n years of daily data (to obtain the n-year average $A_{i,n}$, with i ranging from 2006 to $2019 - n + 1$, in the specific case) over all combinations of contiguous periods (e.g., if $n = 2$, 2006–2007, 2007–2008, etc.; if $n = 3$, 2006–2008, 2007–2009, etc.). Then, we define a "variability index" (VI_n) of the resulting averaged series. We can employ, as a metrics, the average absolute deviation (AAD) of the successive differences, i.e.

$$\mathrm{VI}_n = \frac{1}{(2019 - 2006 - n + 1)} \sum_{i=2006}^{2019-n} |A_{i+1,n} - A_{i,n}| \tag{1}$$

The variability of the n-year averages is represented in Fig. S2 for each lockdown phase (cf. Table 2 in the main text). As can be easily seen, the "roughness" of the series rapidly decreases if a few years are averaged together, then reaches a stable plateau (due to the presence of a trend in the data set). The optimal averaging span depends on the considered lockdown phase, for example the variability is larger and needs a longer average time in winter (phases 1 and 6). A span of 4–5 years is a reasonable choice to avoid large disturbances from short-term weather anomalies while keeping the averaging interval short.

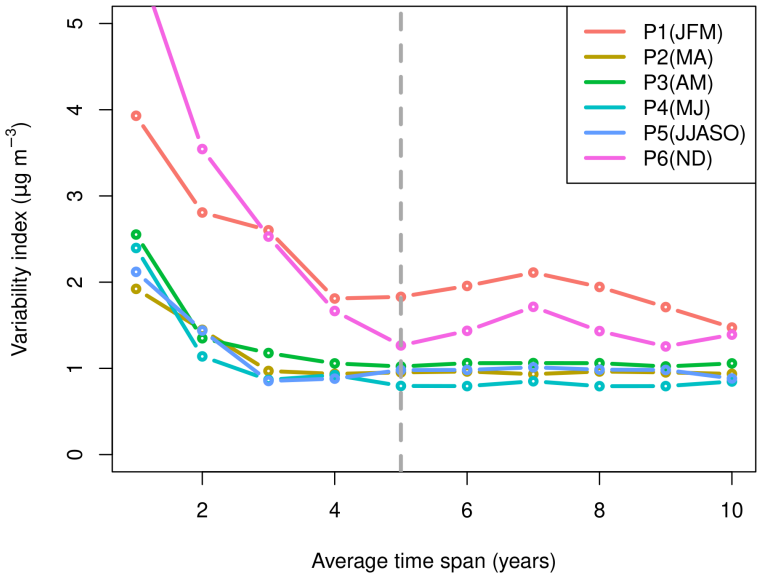

Figure S2. Variability of n-year averages as a function of the time span. The dashed vertical line represents the selected 5-year span. Each line corresponds to a different lockdown phase (cf. Table 2 in the main text, the month initials are reported in parentheses next to the period for better understanding).

For the sake of consistency, i.e. to allow accurate comparison with the average method, a similar 5-year span is used to train the predictive statistical model (Sect. 3.2).

S2. Validation of the predictive statistical model (random forest)

The accuracy of the predictive statistical model is assessed in the following way [3]. Several models are trained for validation purposes over five periods (of 5 years each), i.e. 2010–2014, 2011–2015, 2012–2016, 2013–2017, 2014–2018, and they are compared with real measurements from years 2015, 2016, 2017, 2018, and 2019, respectively. Here we report the mean bias (MB) and the Pearson's correlation coefficient (R), as metrics of the model reliability. The metrics of the comparison show that the model performs well. Indeed, the Pearson's correlation indices between simulations and observations are almost always 0.9 for gases in Aosta–downtown and in Donnas (here with the exception of NO, likely more dependent on the instantaneous traffic fluxes or short-term weather effects), and the mean bias generally amounts to few $\mu g\ m^{-3}$. The complex meteorological and emission conditions in Courmayeur are more difficult to parameterise, however the Pearson's coefficients are still within 0.6 and 0.8. The random forests for PM_{10} perform slightly worse than for gases, likely due to longer particle lifetime and a wider range of sources, but the correlation coefficient is anyway rather large (> 0.7 in most cases).

Table S1. Comparison metrics between measurements and predictions by the statistical model for NO.

Year	Training period	Courmayeur		Aosta–downtown		Donnas	
		MB ($\mu g\ m^{-3}$)	**R**	**MB** ($\mu g\ m^{-3}$)	**R**	**MB** ($\mu g\ m^{-3}$)	**R**
2015	2010–2014	5.8	0.8	4.1	0.9	1.9	0.7
2016	2011–2015	0.2	0.7	10.4	0.9	2.6	0.7
2017	2012-2016	8.8	0.8	1.8	0.9	2.4	0.6
2018	2013–2017	8.5	0.7	13.1	0.8	1.4	0.7
2019	2014–2018	6.4	0.6	3.1	0.9	3.6	0.7

Table S2. Comparison metrics between measurements and predictions by the statistical model for NO_2.

Year	Training period	Courmayeur		Aosta–downtown		Donnas	
		MB ($\mu g\ m^{-3}$)	**R**	**MB** ($\mu g\ m^{-3}$)	**R**	**MB** ($\mu g\ m^{-3}$)	**R**
2015	2010–2014	3.6	0.7	1.6	0.9	0.0	0.9
2016	2011–2015	1.2	0.8	2.3	0.9	2.4	0.9
2017	2012-2016	0.4	0.8	-2.0	0.9	0.0	0.9
2018	2013–2017	8.6	0.6	5.8	0.9	3.7	0.8
2019	2014–2018	8.0	0.7	2.1	0.9	4.5	0.8

Table S3. Comparison metrics between measurements and predictions by the statistical model for O_3.

Year	Training period	Aosta–downtown		Donnas	
		MB ($\mu g\ m^{-3}$)	**R**	**MB** ($\mu g\ m^{-3}$)	**R**
2015	2010–2014	-4.1	0.9	-5.4	0.9
2016	2011–2015	0.5	0.9	-7.1	0.9
2017	2012-2016	-3.4	0.9	-5.6	0.9
2018	2013–2017	0.6	0.9	5.5	0.9
2019	2014–2018	1.5	0.9	-1.5	0.9

Table S4. Comparison metrics between measurements and predictions by the statistical model for $PM_{2.5}$.

Year	Training period	Aosta–downtown	
		MB ($\mu g\ m^{-3}$)	**R**
2015	2010–2014	2.1	0.8
2016	2011–2015	2.1	0.8
2017	2012-2016	-0.7	0.8
2018	2013–2017	3.5	0.7
2019	2014–2018	0.4	0.7

Table S5. Comparison metrics between measurements and predictions by the statistical model for PM_{10}.

Year	Training period	Courmayeur		Aosta–downtown		Donnas	
		MB ($\mu g\ m^{-3}$)	**R**	**MB** ($\mu g\ m^{-3}$)	**R**	**MB** ($\mu g\ m^{-3}$)	**R**
2015	2010–2014	4.0	0.6	3.1	0.8	-0.2	0.7
2016	2011–2015	1.6	0.6	4.4	0.8	1.4	0.7
2017	2012-2016	1.6	0.7	-1.7	0.8	1.2	0.7
2018	2013–2017	5.1	0.4	4.1	0.7	7.5	0.7
2019	2014–2018	4.1	0.4	2.2	0.7	2.2	0.7

S3. Details on the emission inventory and its variations in 2020

The 11 SNAP97 categories related to the types of local emission sources are listed in the following table, according to the European CORINAIR method (e.g., https://www.eea.europa.eu/publications/EMEPCORINAIR5, last access: 22 June 2021).

Table S6. The 11 SNAP97 categories defined by the European CORINAIR method.

Category	Code
Combustion in energy and transformation industries	01
Non-industrial combustion plants	02
Combustion in manufacturing industry	03
Production processes	04
Extraction and distribution of fossil fuels and geothermal energy	05
Solvent and other product use	06
Road transport	07
Other mobile source and machinery	08
Waste treatment and disposal	09
Agriculture	10
Other sources and sinks	11

S4. Details on the meteorological context in 2020 compared to the previous years

The same weather classification introduced in one of our previous studies [4] was used here to easily compare the meteorological patterns in 2020 to the previous years. Figures S3–S5 show the results from the classification, together with detailed information on air temperature and precipitation. It can be noticed that winter periods are generally characterised by wind calm, likely owing to strong temperature inversions in the lowest atmospheric layers and cloudy conditions. In the other periods of the year, the weather is dominated by easterly flows, driven by either the thermal circulation or synoptic forcing, and usually carrying air pollution from the Po basin. Days characterised by westerly winds and precipitation can occur, but they are less systematic – their frequency changing from year to year – and the geographical distribution of precipitation might be very heterogeneous.

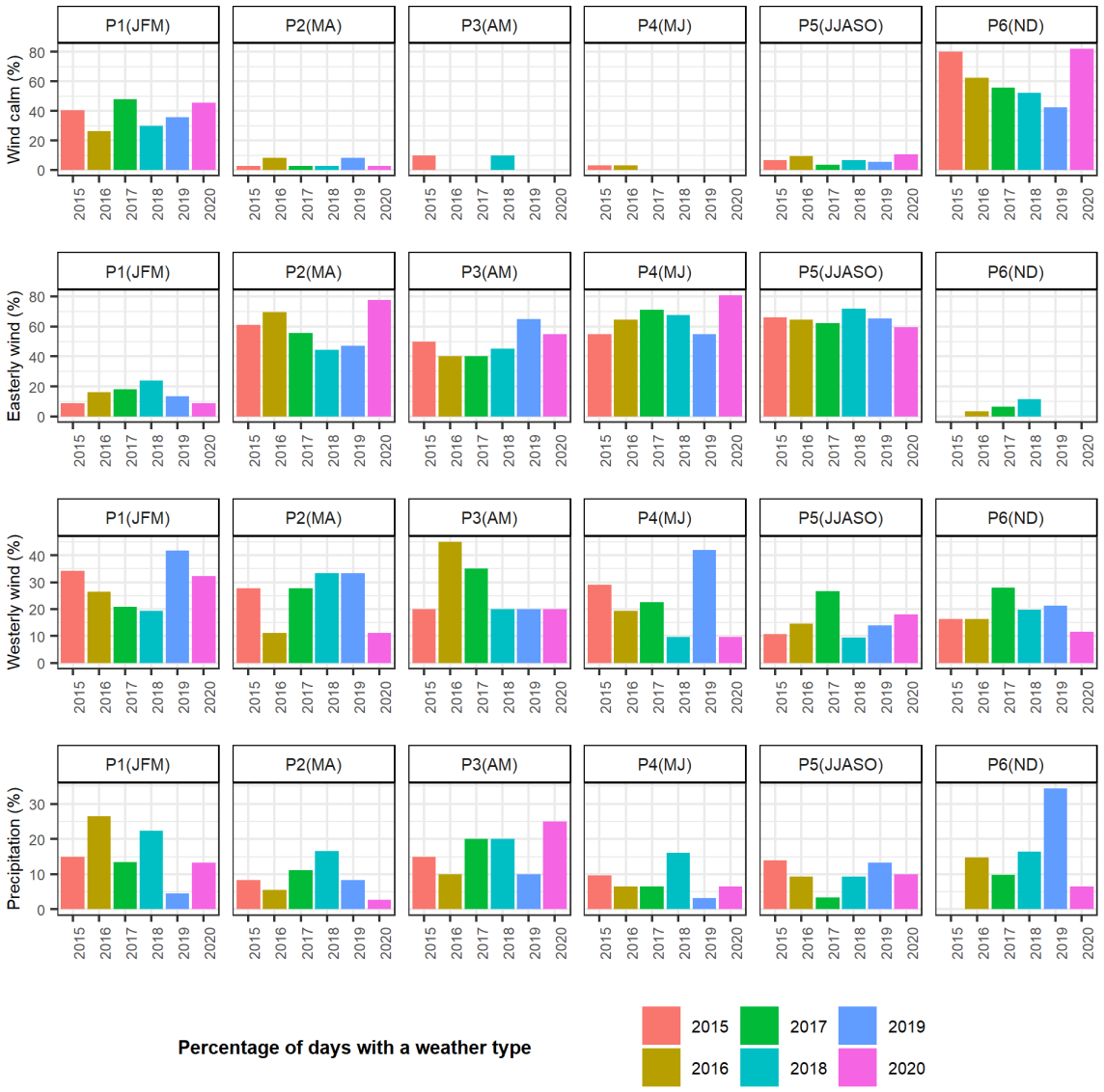

Figure S3. Occurrence of different weather types in the analysed periods for different years. Notice the different range of the vertical scales in the subfigures.

We also show the statistical distributions of the daily average air temperature and the total precipitation in each period.

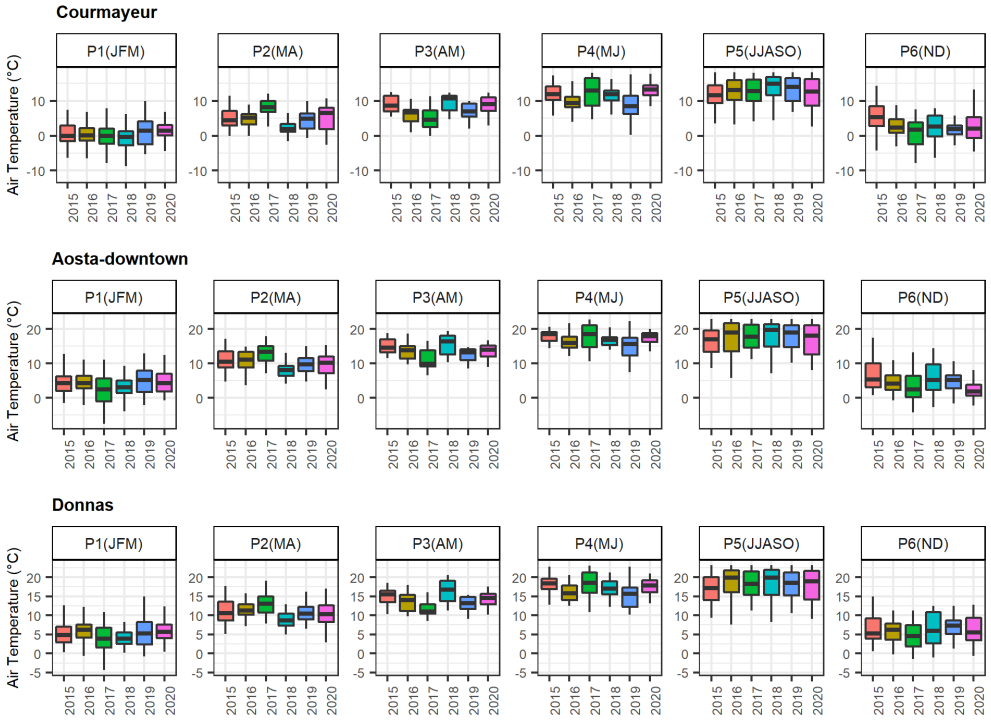

Figure S4. Comparison of daily average air temperature in the analysed periods for different years.

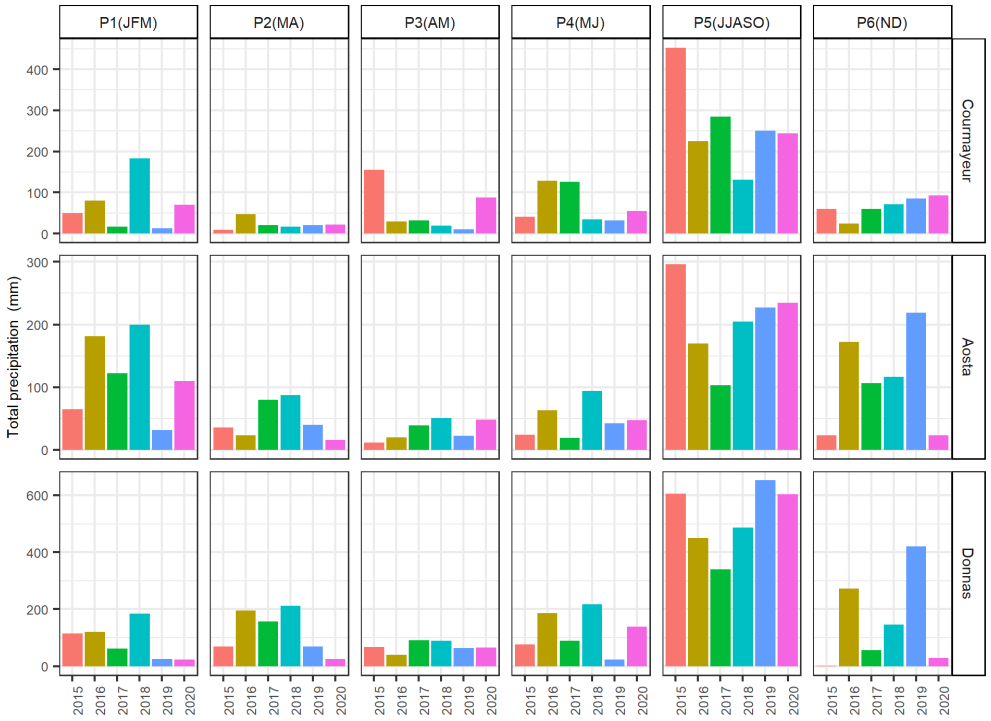

Figure S5. Comparison of total precipitation in the analysed periods for different years.

S5. Details on gaseous pollutant concentrations

The statistical distributions of the daily average concentrations of surface gaseous pollutants measured in the last six years at different air quality stations are shown here below (the respective plot for NO_2 can be found in the main text).

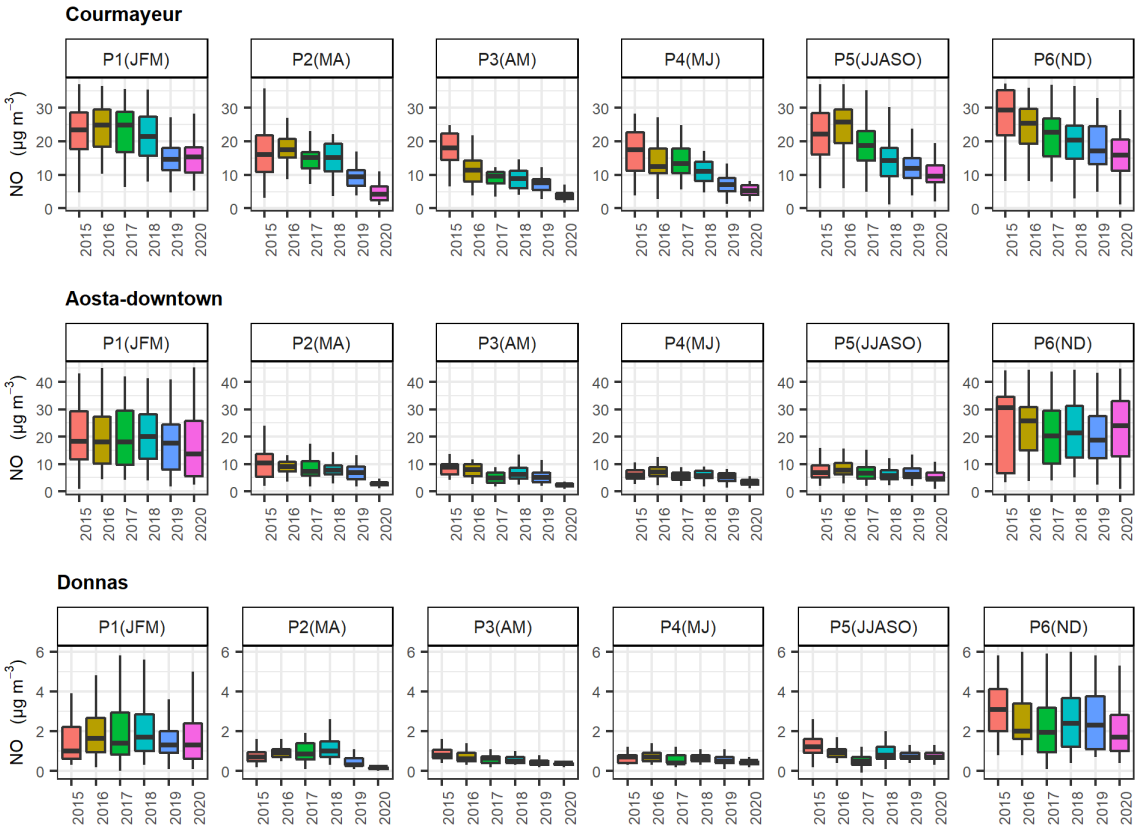

Figure S6. Median (horizontal line in the box), interquartile range (box height), overall variability excluding outliers (vertical line) of daily average NO concentrations measured in each period (cf. definitions in the main text) of the last 6 years at each air quality station. Notice that the ranges of the vertical scale at the three stations are different for better visualisation.

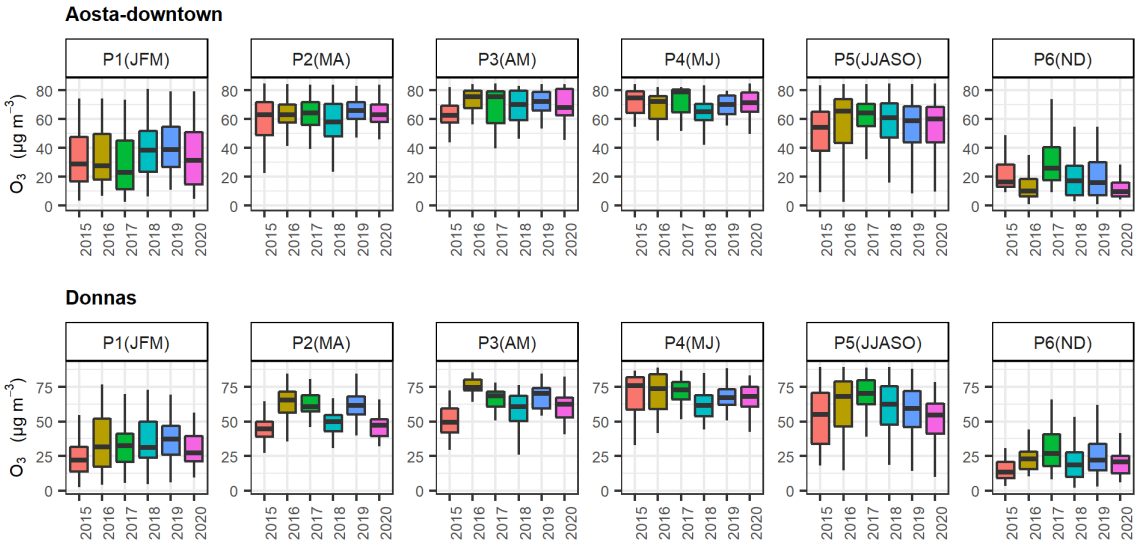

Figure S7. Same as the previous figure, for surface O_3 concentrations. Notice the different ranges of the vertical axes in the panels.

A comparison between actual observations and random forest forecasts (counterfactual scenario accounting for weather effects) is shown here below for each gaseous pollutant and each station. The respective plot for NO_2 can be found in the main text.

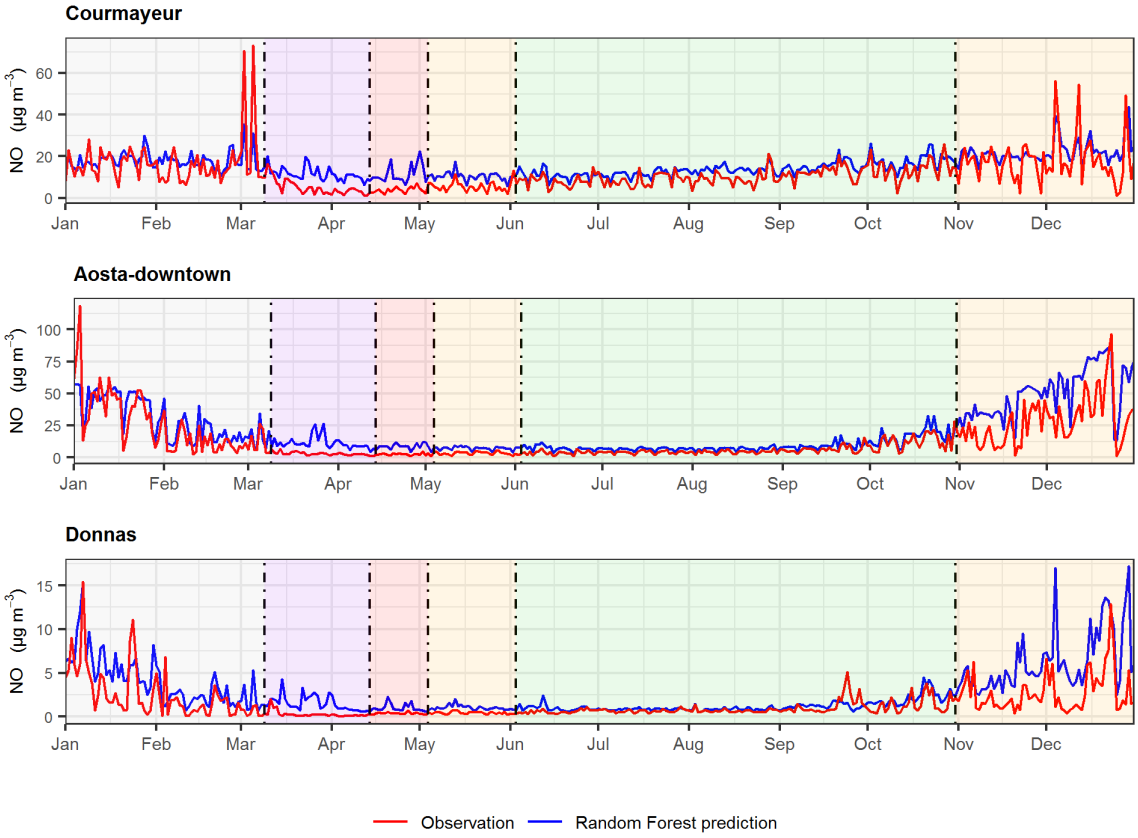

Figure S8. Observation (red) and prediction with the random forest algorithm (blue) of NO surface concentrations for year 2020. The vertical scales are different for ease of visualisation.

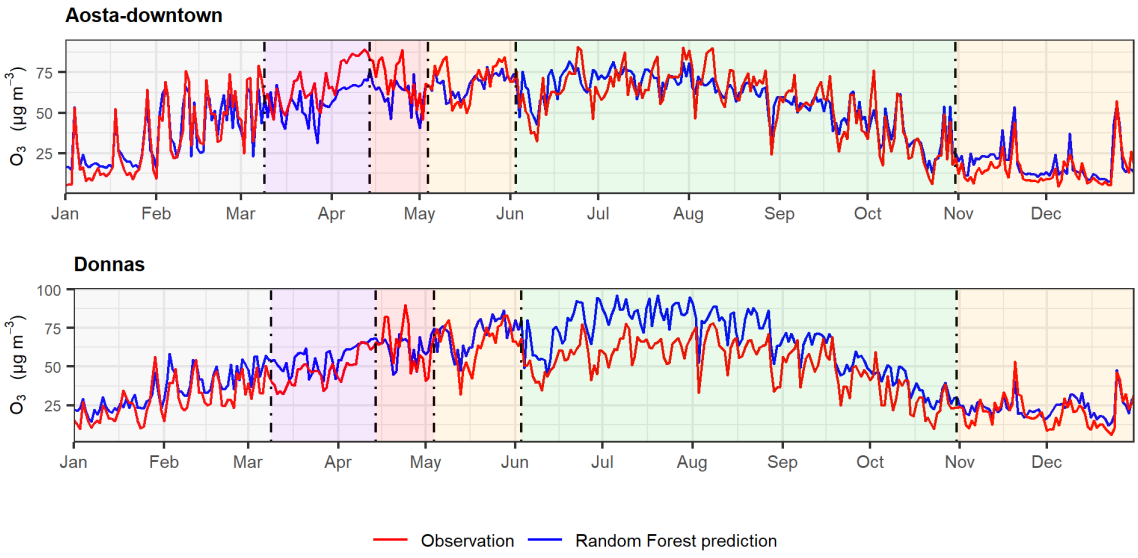

Figure S9. Observation (red) and prediction with the random forest algorithm (blue) of O_3 surface concentrations for year 2020. The vertical scales are different for ease of visualisation.

As an example of the gaseous pollutant evolution over the whole domain, a map of the differences between the NO_2 surface concentrations simulated with the CMT for the curtailed and reference scenarios in each period is presented here below.

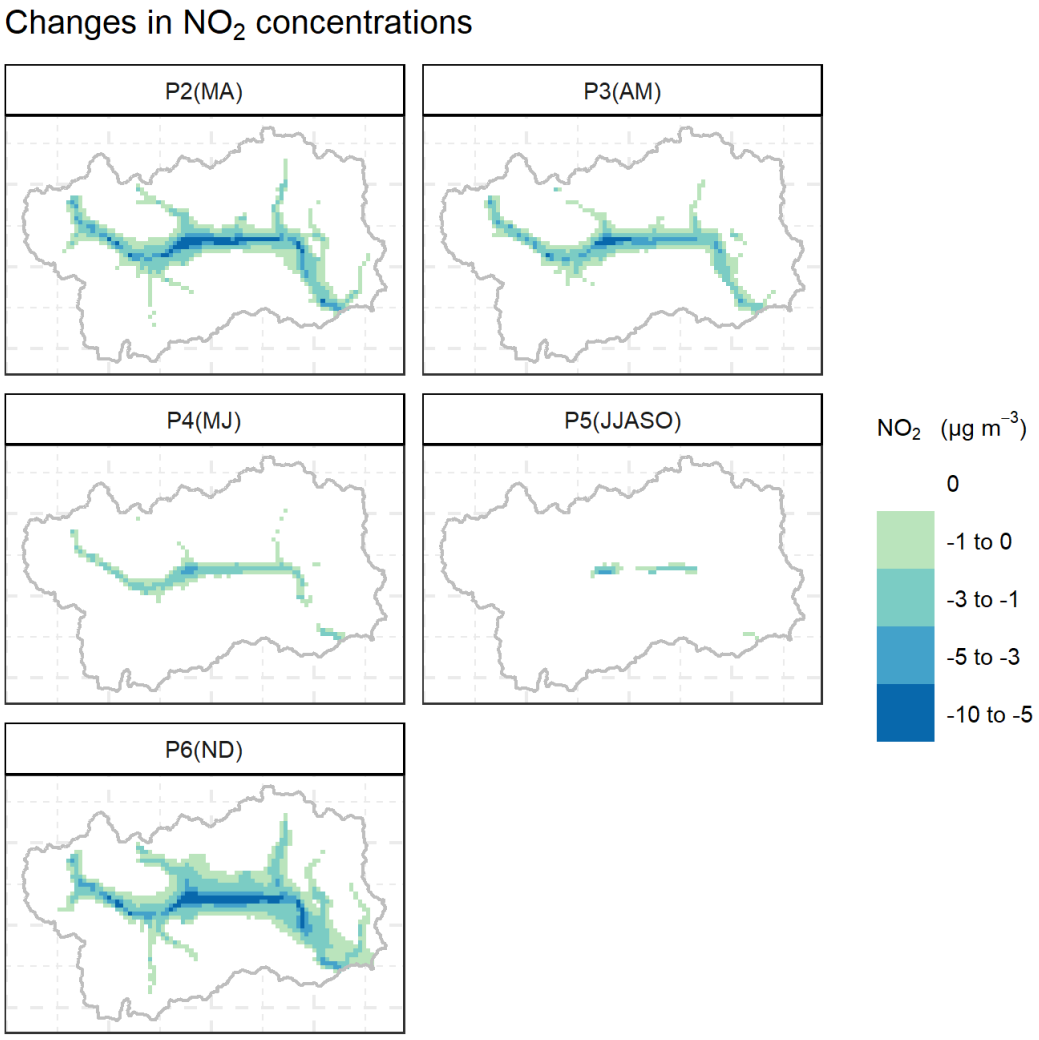

Figure S10. Differences between the NO_2 surface concentrations simulated with the CTM for the curtailed and reference scenarios in each period of the year.

S6. Details on PM concentrations

The following plots represent the statistical distribution of daily average PM concentrations measured in the last six years at different air quality stations.

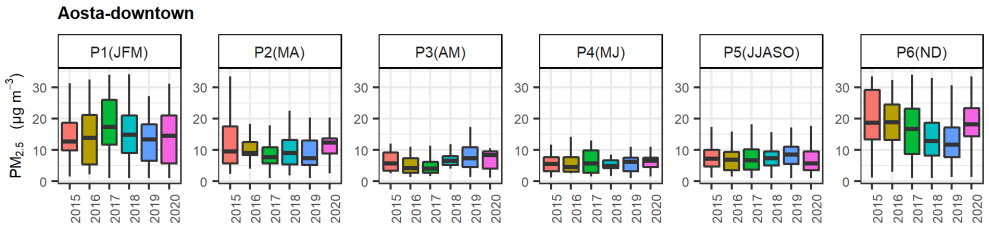

Figure S11. Median (horizontal line in the box), interquartile range (box height), overall variability (excluding outliers) of daily average $PM_{2.5}$ concentrations measured in each period (cf. definitions in the main text) of the last 6 years at each air quality station.

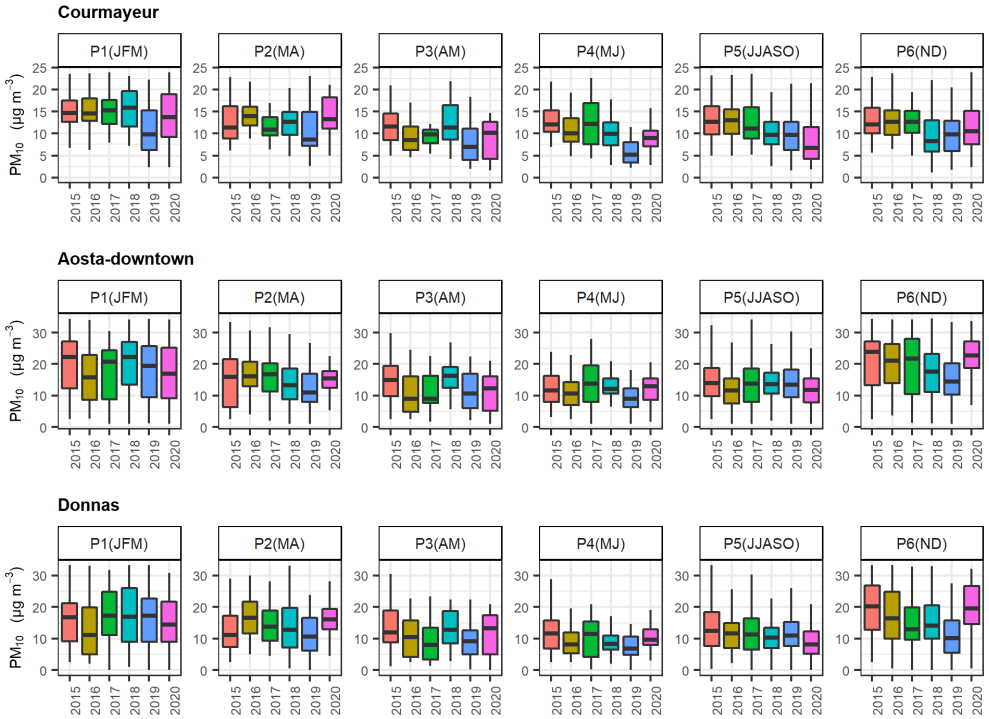

Figure S12. Same as the previous figure for surface PM_{10} concentrations. Notice the difference in the range of the vertical axes.

Here below we represent the actual observations and the random forest forecasts for PM.

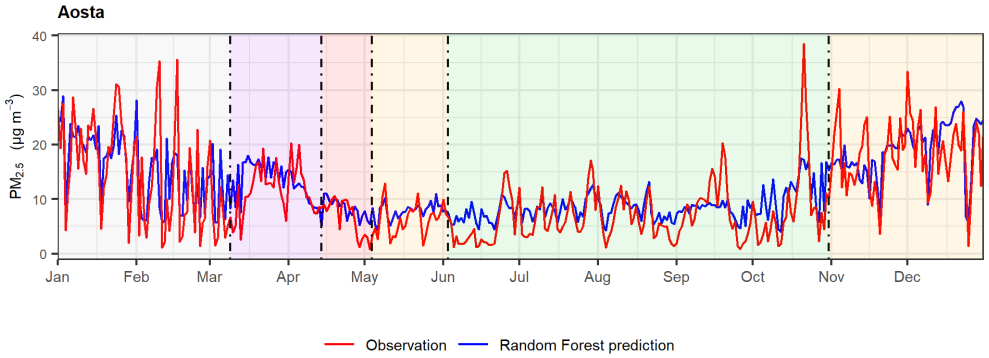

Figure S13. Observation (red) and prediction with the random forest algorithm (blue) of $PM_{2.5}$ surface concentrations in Aosta–downtown for year 2020.

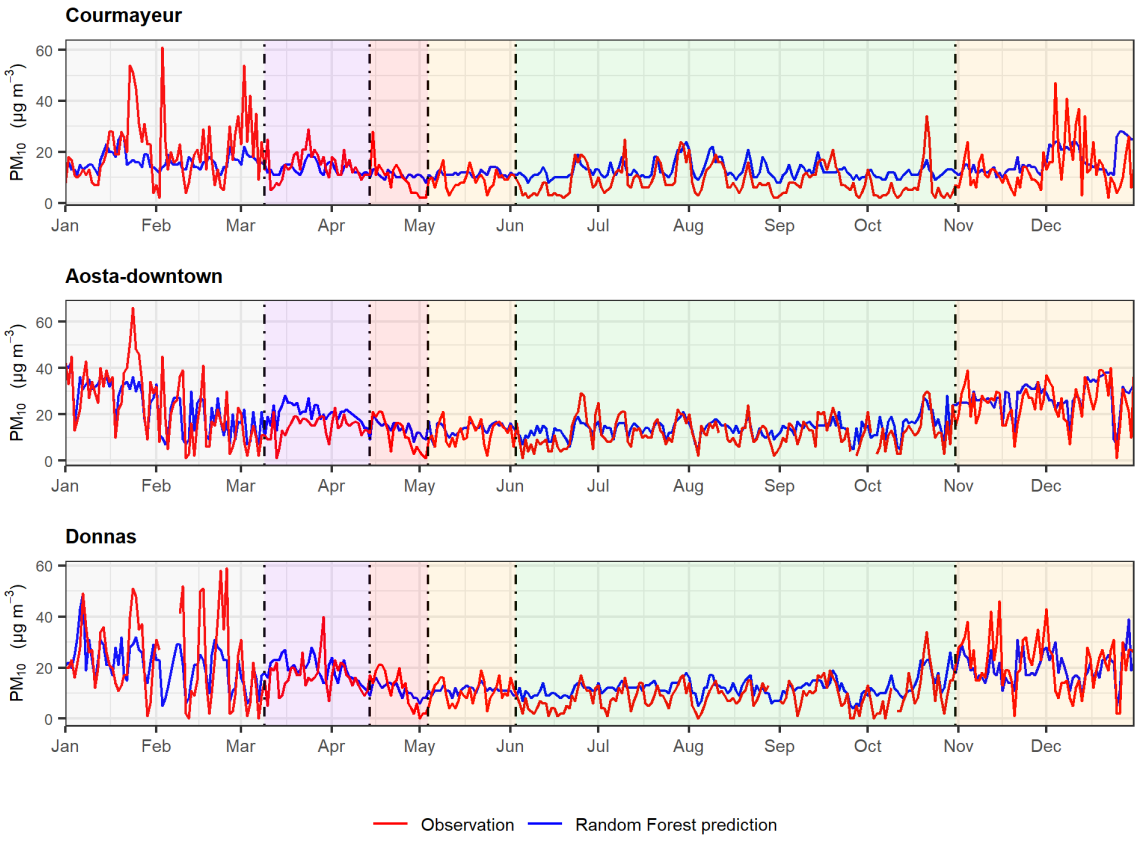

Figure S14. Observation (red) and prediction with the random forest algorithm (blue) of PM_{10} surface concentrations at the different air quality stations for year 2020.

Total reductions in emissions of particulate matter from the inventory, resulting from curtailed emissions sources, are shown in the plot below.

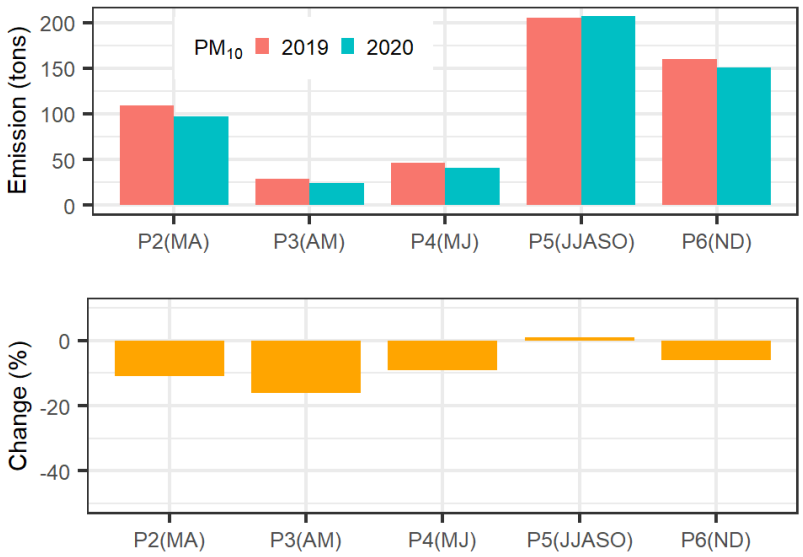

Figure S15. Total PM_{10} emissions in the reference and curtailed scenarios and their percentage reduction over the domain of study. P1 is left unchanged, since it is prior to the lockdown measures. A similar figure for NO_x is provided in the main text.

A map of the differences between the simulated PM_{10} surface concentrations for the curtailed and reference scenarios in each period is presented here below.

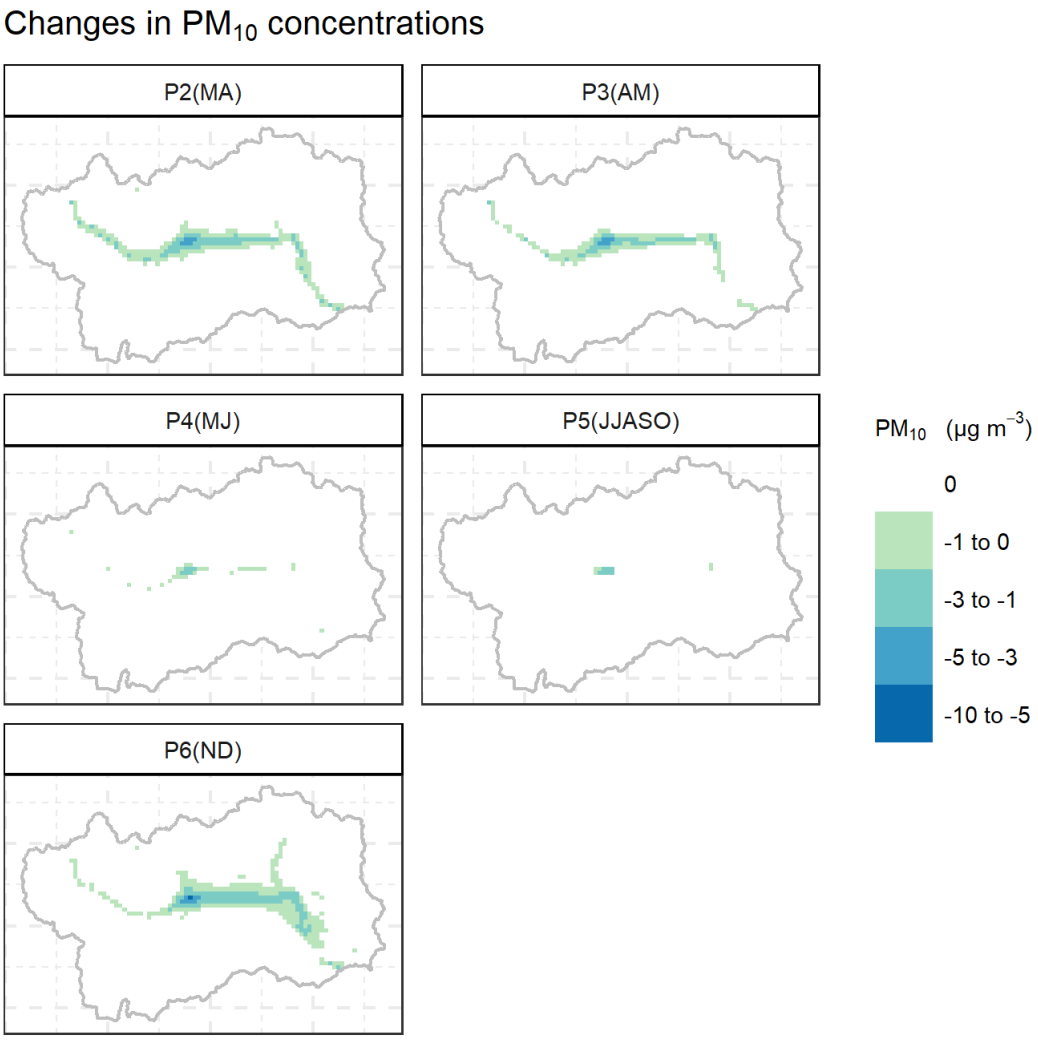

Figure S16. Differences between the simulated PM_{10} surface concentrations for the curtailed and reference scenarios in each period of the year.

S7. Details on aerosol source apportionment

The following plots represent the source profiles from size-PMF at each site where a Fidas200E particle spectrometer is installed. These are remarkably similar at all sampling sites. As already discussed in a previous study [4], the accumulation mode with the smallest size (centred at about 0.2 μm) is linked to particles formed through condensation/coagulation processes and aging ("condensation mode"), such as sulfates transported from the Po basin and aerosol originated locally from traffic exhaust and heating. The slightly larger accumulation mode, centred at about 0.5 μm ("droplet mode"), is representative of the nitrate particles forming in aqueous-phase processes, e.g. in fog during the cold season. The third mode correlates remarkably well with mineral dust deposition, and possibly its resuspension. This is confirmed by comparing its evolution with the results of desert dust forecasts (NMMB/BSC-Dust, http://ess.bsc.es/bsc-dust-daily-forecast, last access: 22 June 2021) and the analysis of back-trajectories, ALC profiles and volume size distributions from the sun/sky radiometer. The mode is centred at about 2 μm, a size consistent with dust dry deposition [5,6]. Finally, the fourth mode is coarse, with sizes up to 10 μm, and is representative of the largest particles such as the ones resuspended from soil and de-icing road salt.

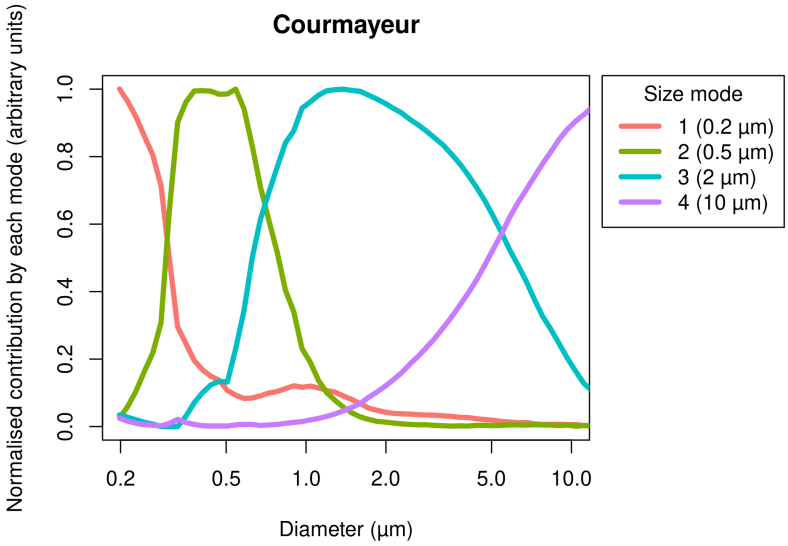

Figure S17. Modes resulting from size-PMF factorisation at Courmayeur in 2018–2020.

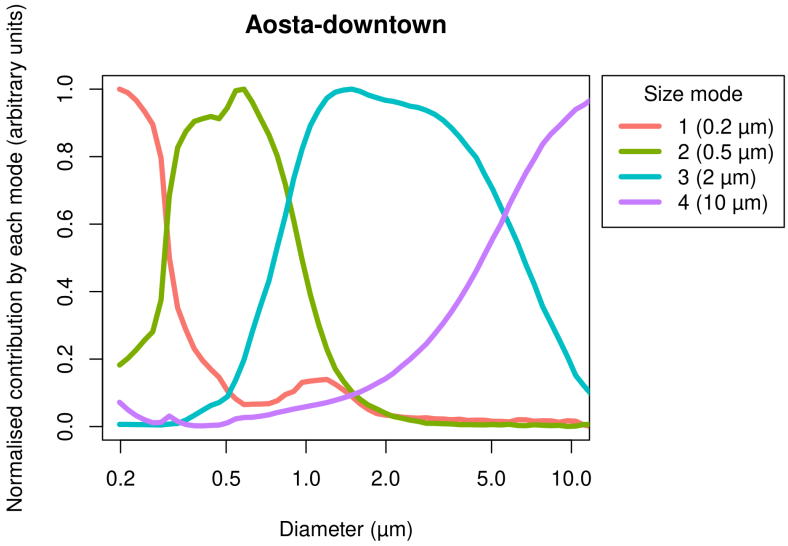

Figure S18. Modes resulting from the size-PMF factorisation at the Aosta–downtown station in 2019–2020.

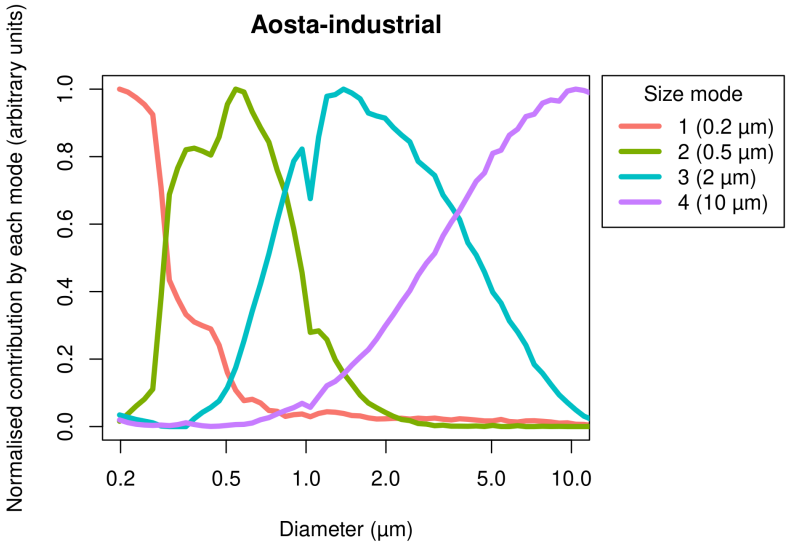

Figure S19. Modes resulting from the size-PMF factorisation at the Aosta–industrial station in 2019–2020.

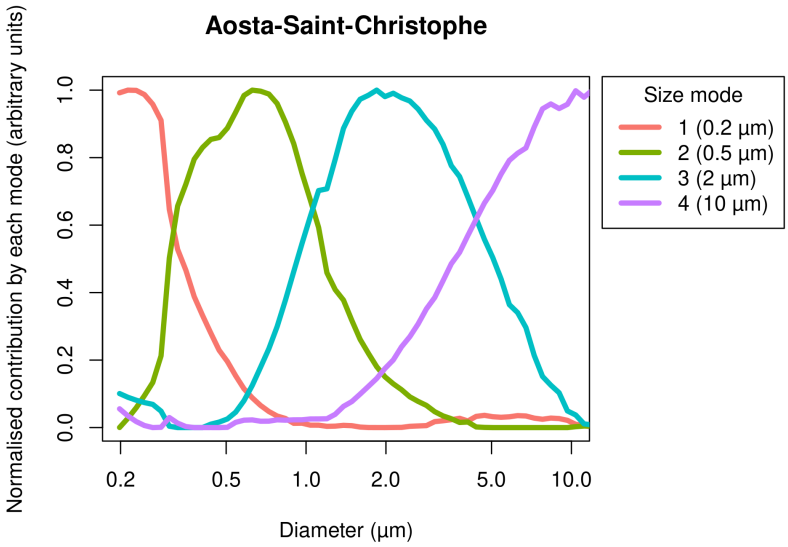

Figure S20. Modes resulting from the size-PMF factorisation at Aosta–Saint-Christophe in 2017–2019.

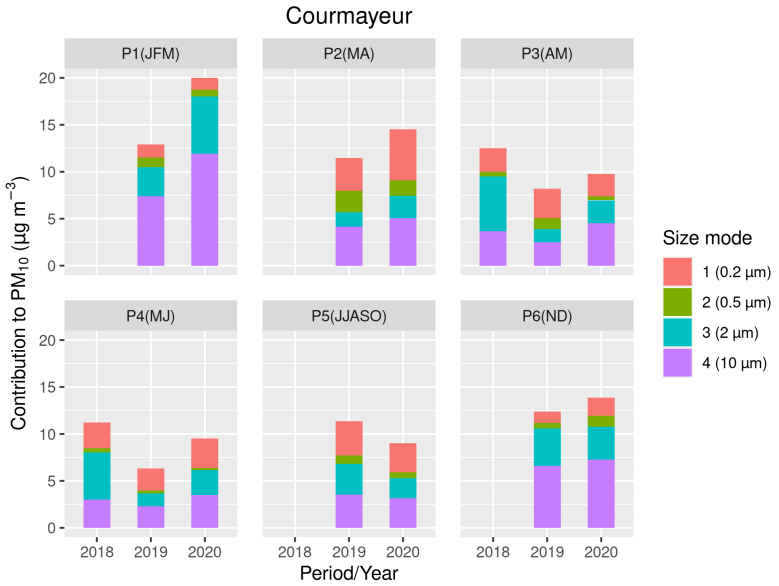

Figure S21. Contribution to the PM_{10} concentration measured at the Courmayeur station by the four modes identified with size-PMF. Only periods with full data coverage are shown in the plot.

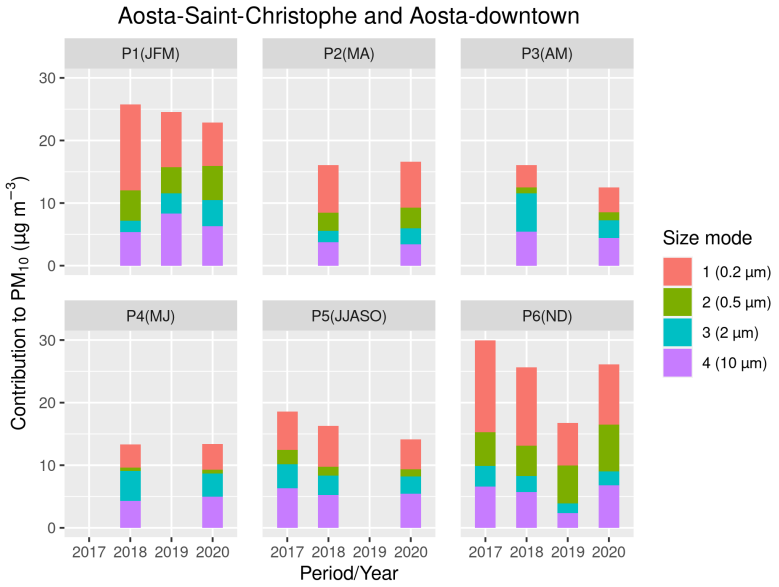

Figure S22. Same as the previous figure for the composite series from Aosta–Saint-Christophe (June 2017–March 2019) and Aosta–downtown (September 2019–2020).

The next figures show the source profiles from chem-PMF in Aosta–downtown using two different factorisations, one based on anion/cations and EC/OC/levoglucosan, and the other based on anion/cation plus metals.

Factors emerging from the first factorisation are (Fig. S23): de-icing road salting (with high concentrations of Na and Cl), biomass burning (high levoglucosan and medium EC and OC), non-biomass burning combustion processes such as traffic/heating (with high EC and NO_x), two modes related to transport of secondary particles from the Po basin (rich in nitrate and sulfate, respectively [4,7]), and a mode rich in crustal elements, such as Ca and Mg. This latter may be connected with both resuspension by traffic/wind and emission from industry. Indeed, oxides of Ca, Si, and Fe originate as slags from the electric arc furnace employed in the steel mill. Moreover, Ca, Si, Al, and Mg oxides form from refining treatments in the ladle furnace. These elements are present in the coarse fraction of fugitive emissions from the industrial plant and are believed to contribute to the "soil" mode at the Aosta–downtown station.

When metals are included in chem-PMF, seven factors arise (Fig. S24): road salt, combustion processes, secondary sulfate, secondary nitrate, soil, and two factors respectively rich in heavy metals (e.g., Cr, Ni, and Mo) from the steel mill, and a Cd- and Pb-rich mode, which was attributed to the industrial sector in a previous study [4]. Cu is found in similar quantities in both traffic and soil modes, which is a possible clue of the contribution of traffic to soil resuspension.

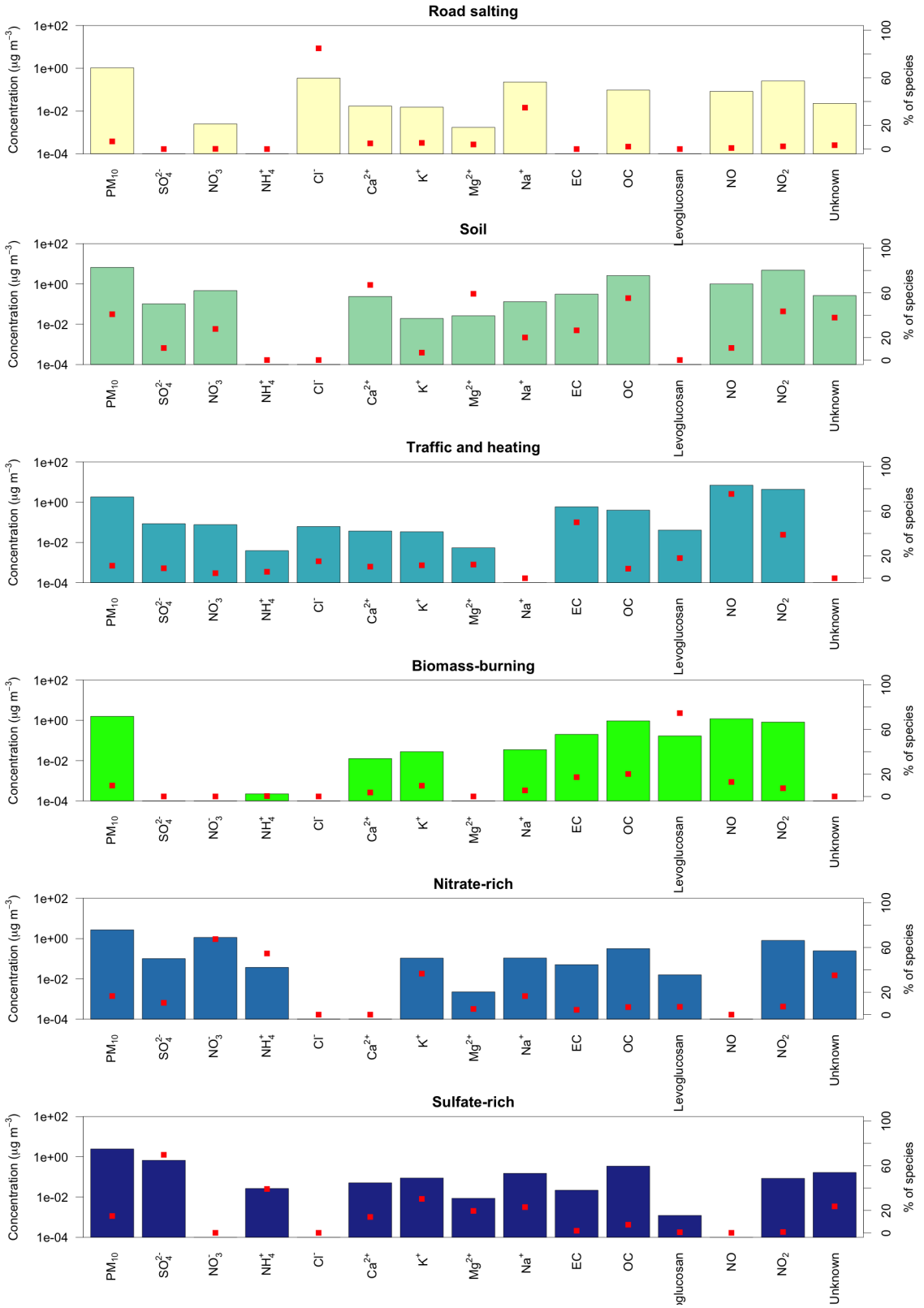

Figure S23. Factor profiles emerging from the anion/cation + EC/OC/levoglucosan chem-PMF. Coloured bars (left axis) represent absolute concentrations, red points (right axis) mark the percentage contribution to each mode of the total for each species.

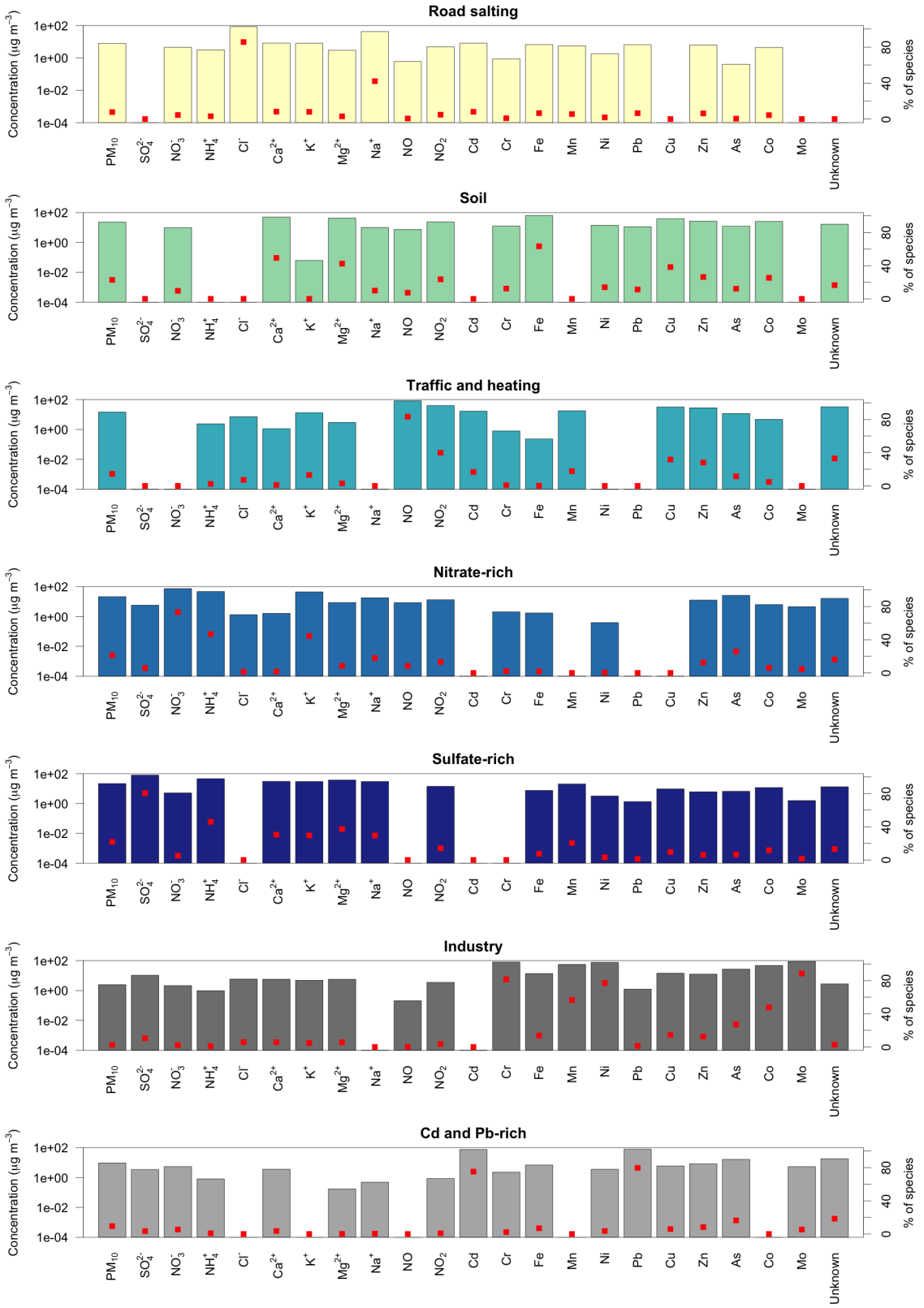

Figure S24. Factor profiles emerging from the anion/cation + metal chem-PMF.

The next figure shows the relative contribution of the biomass burning factor to the $PM_{2.5}$ mass concentration in Aosta–downtown.

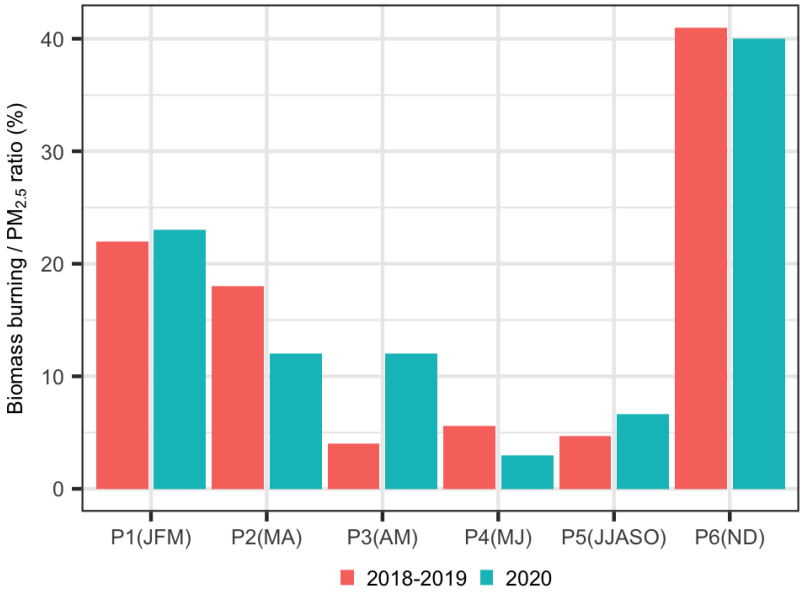

Figure S25. Contribution of the "biomass burning" mode to the PM_{10} concentration in Aosta–downtown from chem-PMF based on anion/cation, EC/OC, and levoglucosan, further normalised using the total $PM_{2.5}$ concentration.

We report here below the estimates of eBC concentrations from the aethalometer data and their optical source apportionment.

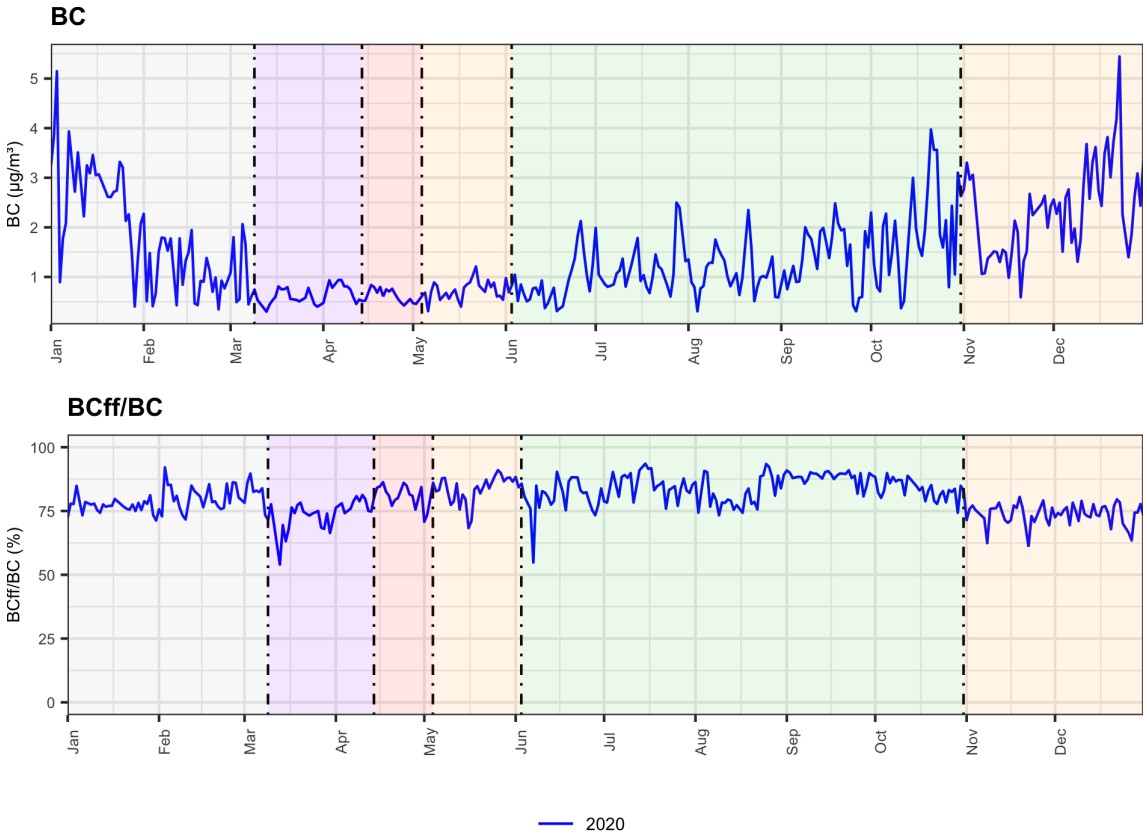

Figure S26. Absolute eBC concentrations measured in Aosta–downtown during 2020 and ratio between the fraction attributed to fossil fuel and total BC.

S8. Results from the sun/sky radiometer

The variations, compared to the average over the previous years, of the aerosol optical depth (AOD) measured at a wavelength of 500 nm by the sun/sky radiometer are shown here below.

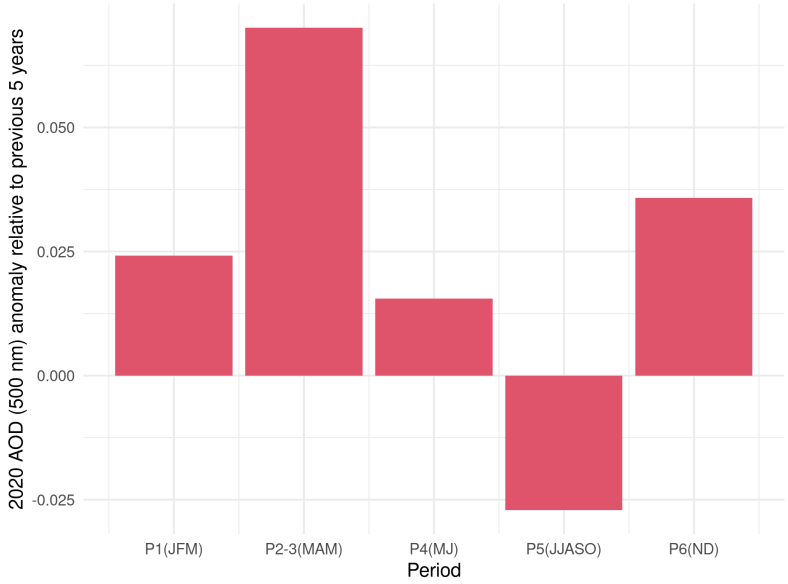

Figure S27. Aerosol optical depth (at 500 nm) absolute anomaly compared to the previous years, as measured by the POM-02 sun/sky radiometer.

References

1. Kroll, J.H.; Heald, C.L.; Cappa, C.D.; Farmer, D.K.; Fry, J.L.; Murphy, J.G.; Steiner, A.L. The complex chemical effects of COVID-19 shutdowns on air quality. *Nat. Chem.* **2020**, *12*, 777–779. doi:10.1038/s41557-020-0535-z.
2. Helsel, D.R.; Hirsch, R.M.; Ryberg, K.R.; Archfield, S.A.; Gilroy, E.J. Statistical methods in water resources. Technical report, Reston, VA, 2020. doi:10.3133/tm4A3.
3. Petetin, H.; Bowdalo, D.; Soret, A.; Guevara, M.; Jorba, O.; Serradell, K.; Pérez García-Pando, C. Meteorology-normalized impact of the COVID-19 lockdown upon NO2 pollution in Spain. *Atmos. Chem. Phys.* **2020**, *20*, 11119–11141. doi:10.5194/acp-20-11119-2020.
4. Diémoz, H.; Gobbi, G.P.; Magri, T.; Pession, G.; Pittavino, S.; Tombolato, I.K.F.; Campanelli, M.; Barnaba, F. Transport of Po Valley aerosol pollution to the northwestern Alps – Part 2: Long-term impact on air quality. *Atmos. Chem. Phys.* **2019**, *19*, 10129–10160. doi:10.5194/acp-19-10129-2019.
5. Nicolás, J.; Yubero, E.; Galindo, N.; Giménez, J.; Castañer, R.; Carratalá, A.; Crespo, J.; Pastor, C. Characterization of events by aerosol mass size distributions. *J. Environ. Monit.* **2009**, *11*, 394–399. doi:10.1039/B813042F.
6. Gobbi, G.; Barnaba, F. Di Liberto, L.; Bolignano, A.; Lucarelli, F.; Nava, S.; Perrino, C.; Pietrodangelo, A.; Basart, S.; Costabile, F.; Dionisi, D.; Rizza, U.; Canepari, S.; Sozzi, R.; Morelli, M.; Manigrasso, M.; Drewnick, F.; Struckmeier, C.; Poenitz, K.; Wille, H. An inclusive view of Saharan dust advections to Italy and the Central Mediterranean. *Atmos. Environ.* **2019**, *201*, 242 – 256. doi:10.1016/j.atmosenv.2019.01.002.
7. Diémoz, H.; Barnaba, F.; Magri, T.; Pession, G.; Dionisi, D.; Pittavino, S.; Tombolato, I.K.F.; Campanelli, M.; Della Ceca, L.S.; Hervo, M.; Di Liberto, L.; Ferrero, L.; Gobbi, G.P. Transport of Po Valley aerosol pollution to the northwestern Alps – Part 1: Phenomenology. *Atmos. Chem. Phys.* **2019**, *19*, 3065–3095. doi:10.5194/acp-19-3065-2019.